　　　　　　　　　　　　　　　　　　　Open Access

Combined effects of pores and cracks on the effective thermal conductivity of materials: a numerical study

Yu-Lin Shen[1]* and Garrett Rose[1]

Abstract

Porous solids are commonplace in engineering structures and in nature. Material properties are inevitably affected by the internal inhomogeneity. The effective thermal conductivity of porous materials has been and remains to be a subject of extensive research. Less attention has been devoted to thermal conductivity impacted by internal cracks. This study is devoted to theoretical analyses of the combined effects of pores and cracks on the effective thermal conductivity. Systematic numerical simulations using the finite element method are performed based on two-dimensional models, with periodic distributions of internal pores and cracks. The parametric investigations seek to address how individual geometric layout can influence the overall thermal conduction behavior. In addition to circular pores and isolated cracks, angular pores with cracks extending from their sharp corners are also considered. It is found that both isolated cracks and cracks connected to existing pores can significantly reduce the effective thermal conductivity in porous materials. Since it is much easier to microscopically detect internal pores than thin cracks, care should be taken in using the apparent porosity from microscopic images and density measurements to estimate the overall thermal conductivity. Quantitative analyses of the detailed geometric effects are reported in this paper.

Keywords Thermal conductivity, Porous material, Finite element analysis, Crack, Additive manufacturing

Introduction

Heterogeneous materials are ubiquitous in nature and in engineered structures. Their physical properties can be significantly influenced by local heterogeneities and defects. One form of heterogeneity is porosity, and in such materials, distinct features of the solid phase and void space exist. Conductive heat flow inside the material is thus impeded and diverted by porosity, causing a reduction of effective thermal conductivity compared to its pure solid counterpart (Kaviany 1991; Bauer 1993; Smith et al. 2013; Pietrak and Wisniewski 2015). The thermal conduction behavior plays a critical role in a wide range of engineering applications including nuclear fuel components (Bakker et al. 1995; Bai et al. 2016; Hawkes et al. 2017; Iasir et al. 2018; Wang and Zhao 2021); energy storage systems (Dinesh and Bhattacharya 2019); thermal barrier coatings (Gu et al. 2001; Renteria et al. 2006; Zhu et al. 2019); thermal insulation (Lu et al. 1998; Amran et al. 2015; Dou et al. 2019); electronic packaging (Ogushi et al. 2004; Zhao et al. 2019; Sun et al. 2024); and compact heat exchangers (Yeap et al. 2013). In additively manufactured materials, defects such as voids normally exist or they may be designed for physical media flow. Heat conduction for additively manufactured materials is essential due to the local elevated-temperature processes and the resulting porosity in the fabricated products (Zhang et al. 2018; Ibrahim et al. 2020; Ghorbani et al. 2022; Yap et al. 2023).

Internal macroscopic or microscopic cracks may be considered a special form of porosity in solids. Although

*Correspondence:
Yu-Lin Shen
shenyl@unm.edu
[1] Department of Mechanical Engineering, University of New Mexico, Albuquerque, NM 87131, USA

there is essentially no bulk void volume associated with an internal crack, each crack still represents a discontinuity for thermal conduction. Compared to the pure solid counterpart, the effective thermal conductivity of a crack-containing media will be reduced (Hasselman 1978; Hoenig 1983; Benveniste and Miloh 1989; Kushch and Sangani 2000; Sevostianov 2006; Nguyen et al. 2017; Rangasamy Mahendren et al. 2020). Various analytical expressions, either model-based or empirical, describe the effect of porosity on the effective thermal conductivity (Maxwell 1873; Rayleigh 1892; Landauer 1952; Loeb 1954; Hashin and Shtrikman 1962; Schulz 1981; Chiew and Glandt 1983; Bauer 1993; Ordonez-Miranda and Alvarado-Gil 2012; Yang et al. 2013; Smith et al. 2013; Pietrak and Wisniewski 2015; Kiradjiev et al. 2019). A large spread of predictions however exists, with some models being specific to certain porous configurations. Computational approaches such as the finite element method (Bakker et al. 1995; Iasir et al. 2018; Wang and Zhao 2021; He et al. 2019; Xu et al. 2021) can also be employed for such prediction. The numerical results were generally used for obtaining trends, elucidating theoretical and analytical solutions, and assisting in two- and three-dimensional conversions, etc. While analytical and numerical studies of effective thermal conductivity provided insights for porous and crack-containing materials (separately), one scenario has not been systematically studied: materials with coexisting internal pores and cracks. Typical porous structures may also contain distributed cracks, which is expected to further reduce the effective thermal conductivity. Examples include nuclear fuels (Kubota et al. 1964), sintered materials (Qin et al. 2020), and geological materials (Rutqvist et al. 2002). Furthermore, in additively manufactured materials, both voids and cracks caused by lack of fusion are commonplace (Bidare et al. 2022; Hashemi et al. 2022; Byun et al. 2024). When individual voids take an angular rather than rounded shape, cracks may also be expected to form at the sharp corners. Note that, compared to regular porosity, cracks are much more difficult to detect in a microscopic image or from density measurement. How these "hidden" cracks may further degrade the thermal conductivity of a porous material requires fundamental studies. The present work provides such a systematic numerical assessment under the condition of periodic distributions of cracks in addition to pores.

Although larger-scale numerical simulations incorporating many pores or actual image-based pore geometries may be employed (Bakker et al. 1995; Carson et al. 2003; Kaddouri et al. 2016; Iasir et al. 2018; Bowen et al. 2020; Wang and Zhao 2021; Zhang et al. 2021; Marr et al. 2022), the results generally pertain to the specific regular or irregular geometries and may not offer sufficient insight into how local arrangement of pores actually dictates the overall behavior. The "unit-cell" approach assuming a periodic arrangement of microconstituents is an alternative (Hsu et al. 1995; Ogushi et al. 2004; Yvonnet et al. 2008; Xiong et al. 2022). Our previous analyses thus used this approach and considered simple geometric models with easy tuning of geometric parameters, in order to systematically pinpoint the connection between microscopic (shape, size and spatial distribution of pores) and macroscopic (effective composite behavior) features (Shen et al. 2022a). It was found that the effective thermal conductivity is insensitive to the spatial arrangement of circular and spherical pores, and the same insensitivity also holds true for clustering and a mixture of pore sizes. In a subsequent study, the effects of internal cracks (no pores) using similar types of geometric arrangement were analyzed (Shen et al. 2022b). The effective conductivity was found to be insensitive to the actual crack arrangement and can be uniquely represented by the ratio of crack size to the unit-cell size of the model. The periodic crack configurations were also seen to be representative of random sizes, orientations, and spatial distributions of cracks, thus exhibiting a high degree of generality. The present work builds on the previous efforts mentioned above, to incorporate *both* pores and cracks into the analyses, and further explore the effects of cracks extended from the existing pores.

The remainder of this paper is organized into the following sections. The numerical model descriptions and simulation approach are introduced in the "Numerical model description" section. The "Preliminary results: separate effects of periodic pores and periodic cracks" section provides representative results from the two previous studies mentioned above (one figure replotted from each study (Shen et al. 2022a, 2022b), for laying the foundation for the new analyses in subsequent presentations. The "Combined effects of periodic pores and cracks" section reports new findings from the combined pore/crack models. To test the generality of the periodic geometric arrangements, more random pore/crack distributions are considered in the "More random distributions" section. The "Cracks extended from angular pores" section focuses on several scenarios of pores with sharp corners where cracks exist. General conclusions are given in the "Conclusions" section. Attention in this work is devoted to two-dimensional models only. Three-dimensional simulations will involve exceedingly complex geometric possibilities and will be left as future work.

Numerical model description

The current study focuses on the coexistence of pores and cracks in a solid material. The geometric models are built upon 2D distributions of pores (without cracks) and

cracks (without pores), so these reference configurations are first introduced. Representative results for these separate analyses will be shown in the "Preliminary results: separate effects of periodic pores and periodic cracks" section, with data taken from our previous numerical studies for pores only (Shen et al. 2022a) and cracks only (Shen et al. 2022b).

Pores-only and cracks-only models

Figure 1a shows the baseline porous model with a square array of circular pores. The shaded circles represent the empty space surrounded by a solid matrix. Because of the existence of symmetry and periodicity, the highlighted squares (unit cells) are the actual domains needed for the numerical analyses. Temperature gradient can
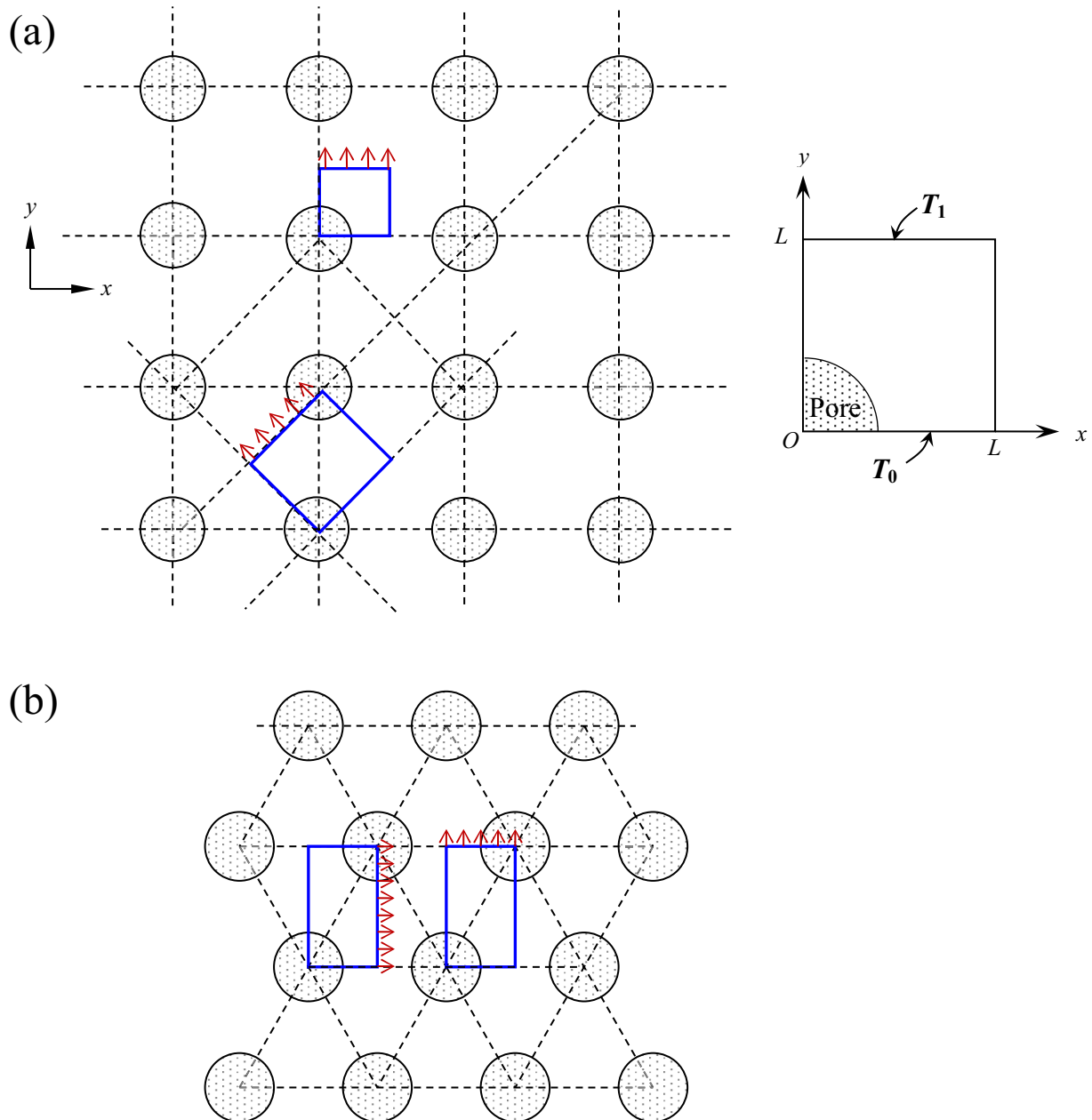

Fig. 1 Schematics showing the square array (**a**) and the hexagonal array (**b**) of circular pores of uniform size. The shaded circles represent the pores, and the highlighted squares or rectangles (unit cells) are the actual domains needed for the simulations, with the arrows representing the temperature gradient directions of 0/90° and 45°. In (**a**) a representative unit cell used for the actual modeling of square-array 90° conduction is also shown, with constant temperatures T_1 and T_0 imposed on the top and bottom boundaries, respectively

be prescribed along the 0/90° directions (same results for these two directions) and along the 45° direction, as represented by the small arrows. Figure 1a also shows a typical micromechanical unit cell. With appropriate boundary conditions imposed, a single cell effectively represents an infinite array of microstructures. In the absence of heat source, the governing equation is

$$K_m \left(\frac{\partial^2 T}{\partial x^2} + \frac{\partial^2 T}{\partial y^2} \right) = 0, \tag{1}$$

where K_m is the thermal conductivity of the solid matrix and T is temperature. For simulating the steady-state heat conduction along the y-direction, for instance, constant temperatures of T_0 and T_1 (with $T_1 > T_0$) are imposed on the horizontal boundaries $y = 0$ and $y = L$, respectively. The Neumann adiabatic boundary conditions are enforced on the side boundaries $x = 0$ and $x = L$ with temperature gradient in the x-direction prohibited, due to symmetry. The effective thermal conductivity of the pore-containing structure, K_{eff}, is then

$$K_{\text{eff}} = \frac{JL}{T_1 - T_0}, \tag{2}$$

where J is the total reaction heat flux obtained from the simulation. Note that when there is no pore and no crack in the model, $K_{\text{eff}} = K_{\text{m}}$. It is worth mentioning that empty space may be used in the model to represent the pore, or one may treat the pore as a second-phase particle with a zero thermal conductivity (which essentially represents an air bubble). Both approaches generate the same numerical results. In other engineered and geological materials, internal pores may also contain various fluids (Atabaki and Baliga 2007; Abdulagatova et al. 2010; Zhou et al. 2016). While these material systems are beyond the scope of the present work, the same modeling methodology can be employed for analyzing their thermal conduction behavior.

For examining the model generality, an alternative hexagonal arrangement is considered in Fig. 1b. Two rectangular unit cells are highlighted, where all their side boundaries are symmetry lines of the global periodic structure. The case with small horizontal arrows signifies not just the x-direction conduction but also along the ±60° directions, meaning that this particular unit-cell model encompasses all three orientations with the nearest-neighbor pores. The rectangular unit cell with small vertical arrows, on the other hand, represents conductions along the y-direction as well as the ±30° directions, namely all three orientations with pores having the second-nearest neighbors. As a consequence, the hexagonal arrangement in Fig. 1b effectively features every possible 30° direction in the entire 360° span.

For studying the effect of internal cracks, numerical models of periodic geometric arrays are also utilized. Figure 2a shows equal numbers of cracks oriented along the x- and y-directions in an alternate fashion, with the crack centers placed in a square alignment. For easy visualization, cracks are depicted as sharp ellipses. In Fig. 2b, the crack centers form a staggered array. Both cases will lead to the same effective thermal conductivity along the x- and y-directions. The squares highlighted in Figs. 2a and b have all their side boundaries being the symmetry lines, so they are the unit cells needed in actual simulations as shown in Fig. 2c. The same methodology is used to calculate the effective thermal conductivity as described above. The side lengths of the cells are different for different models, for the purpose of keeping one full crack per area of L^2 in all cases thus ensuring valid comparisons of the effective thermal conductivity. For example, in the middle unit cell in Fig. 2c, there is a net "half-crack" within an area of $L^2/2$ so the crack density is $1/L^2$. When presenting the numerical results, the quantity a/L is used to represent the normalized crack size, where "a" denotes the half crack length (Shen et al. 2022b).

Models with mixed pores and cracks

Numerical results for the pores-only and cracks-only models are presented in in the preliminary results section below, and it will be shown that the reduction in effective thermal conductivity is insensitive to the spatial distribution of pores and cracks. Therefore, to study the combined effect of pores and cracks, the simple square array is used as a basis to construct the geometric models. Figure 3a shows the first distribution which is a combination of Figs. 1a and 2a. The highlighted square-shaped unit cell is the actual domain needed for the simulations, with global symmetry across all the unit cell's side boundaries. One can define the crack density D_c and pore density D_p, and in this case, their relation is $D_c = D_p$ since there is one full pore and one net crack in each unit cell. The second configuration is shown in Fig. 3b, which is a combination of Figs. 1a and 2b. Note that, with the staggered arrangement of cracks, $D_c = 0.5\ D_p$ in this case. Highlighted in Fig. 3b are two unit cells with all their boundaries being symmetry lines. Figure 3c includes all three unit cells. The side lengths of the cells are chosen such that there is one circular pore per area of L^2 in all cases while keeping one full crack and one-half crack per L^2 for the configurations in, respectively, Figs. 3a and b.

For the purpose of checking if the periodic unit-cell approach in Fig. 3 is representative of realistic microstructures, random distributions of pores and cracks are also considered. More random models with the pore area fractions, f_p, of 0, 0.1, and 0.2 are constructed, with either $D_c = D_p$ or $D_c = 0.5\ D_p$.
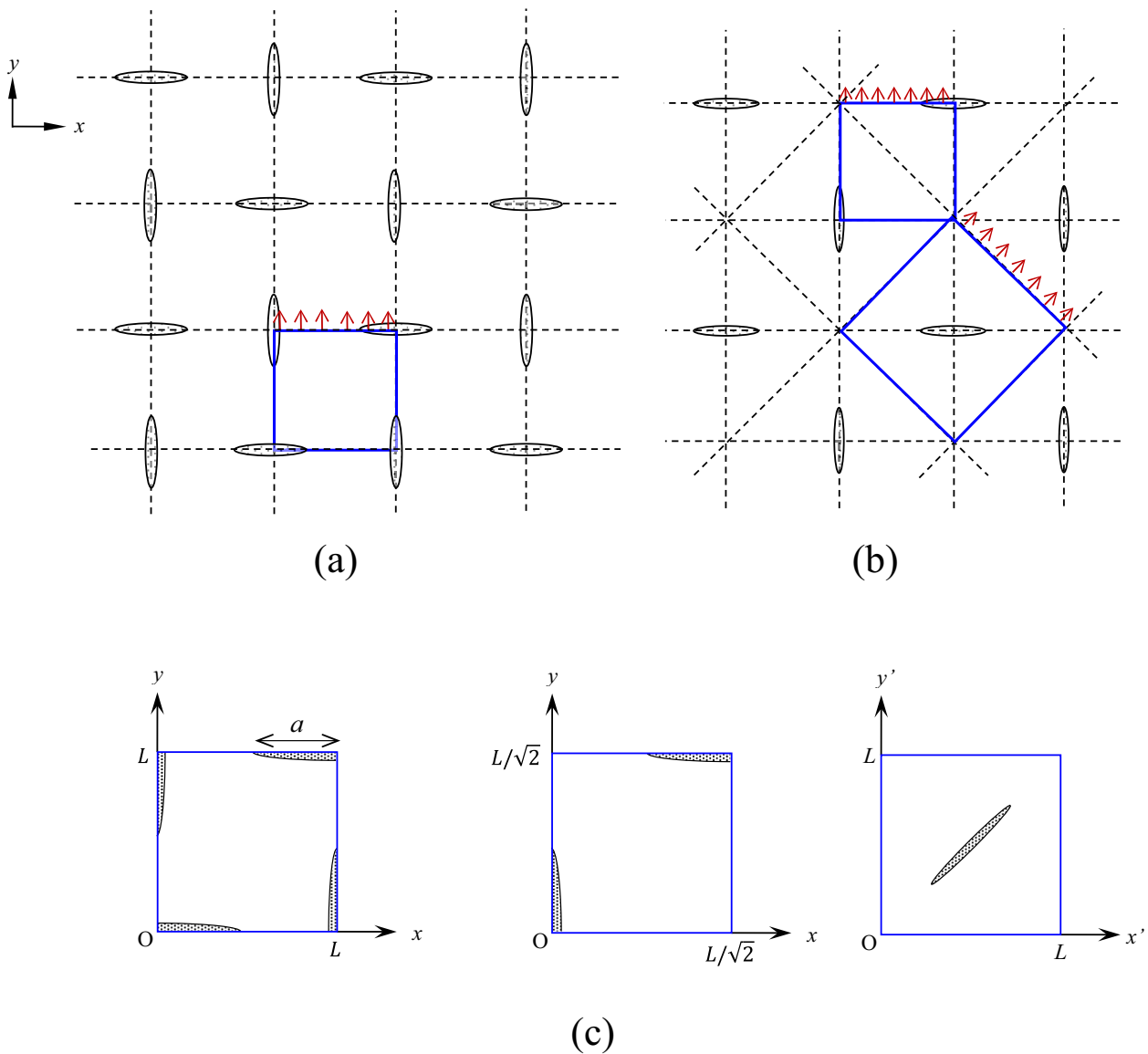
Fig. 2 Schematics showing cracks with mixed orientations in an aligned square array (**a**) and cracks with mixed orientation in a staggered array (**b**). For better visualization, cracks are shown as sharp ellipses. The arrangements result in equal effective thermal conductivity along the *x*- and *y*-directions. The square-shaped unit cells highlighted in (**a**) and (**b**) are those used in actual simulations as shown in (**c**). The side lengths of the cells are different for different models, for the purpose of keeping one full crack per area of L^2 in all cases and thus ensuring valid comparisons of the effective thermal conductivity

An example of $D_c = 0.5\, D_p$ is shown in Fig. 4, where six pores and three cracks of various sizes exist in a $3L \times 3L$ domain, with the total $f_p = 0.2$ and average normalized crack size of $a/L = 0.29$. Note that the effective conductivity values along the *x*- and *y*-directions for such types of random models are essentially the same. The resulting effective thermal conductivity will be compared with the periodic unit-cell analyses.

Cracks extended from pores

In this study, another form of coexisting pores and cracks is considered, where cracks are initiated from the sharp corners of each pore. Figures 5a and b show the model geometries based on diamond-shaped (rotated square) pores and square pores, respectively. Note that the general configuration in Fig. 5a is frequently observed in polymers additively manufactured by fused filament
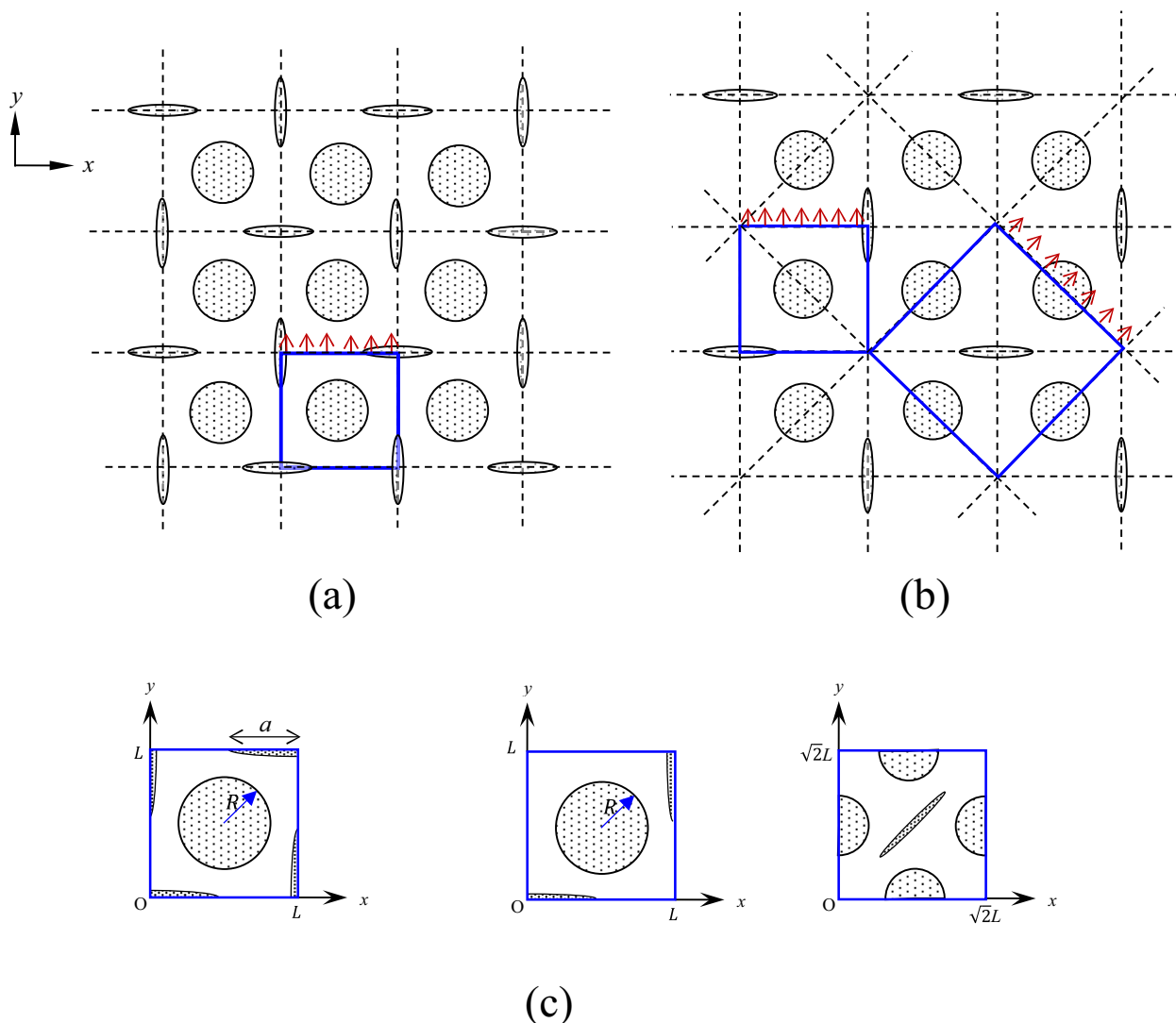
Shen and Rose *J Mater. Sci: Mater Eng.* (2024) 19:25

Page 6 of 19

Fig. 3 Schematics showing periodic unit-cell models of coexisting circular pores and cracks, with crack density being the same as pore density ($D_c = D_p$) (**a**) and crack density being one-half of pore density ($D_c = 0.5D_p$) (**b**). Note that in (**a**) the cracks are of mixed orientations in an aligned square array as in Fig. 2a, and in (**b**) the cracks are of mixed orientations in a staggered array as in Fig. 2b, while the pores are assumed to be in a simple square array. The square-shaped unit cells highlighted in (**a**) and (**b**) are those used in actual simulations as shown in (**c**). The side lengths of the cells are different for different models, for the purpose of keeping one circular pore per area of L^2 in all cases, while keeping one full crack and one-half crack per L^2 in, respectively, (**a**) and (**b**)

fabrication, where many visible aligned voids exist due to poor filling of the filament rasters (Sun et al. 2008; Rankouhi et al. 2016; Ghorbani et al. 2022). Such materials may also exhibit a relatively weak inter-filament strength causing crack formation. In each of Figs. 5a and b, two separate unit-cell models of the aligned (0/90°) and staggered (45°) arrangements can be identified and used in actual simulations. The aligned diamond shape (Fig. 5a), staggered diamond shape (Fig. 5a), aligned square (Fig. 5b), and staggered square (Fig. 5b) are henceforth referred to as models of AD90, SD45, AS90, and SS45,

respectively. The primary objective is to quantify (i) how the pores and associated cracks degrade the effective thermal conductivity from one extreme (four-sided pores only) to the other extreme (cross-shaped cracks only), and (ii) the effect of the relative sizes of the pore/crack combination.

All simulations described in the "Pores-only and cracks-only models," "Models with mixed pores and cracks," and "Cracks extended from pores" sections were carried out using the finite element software ABAQUS (VIAS3D ACADEMIA, Houston, TX, USA). The
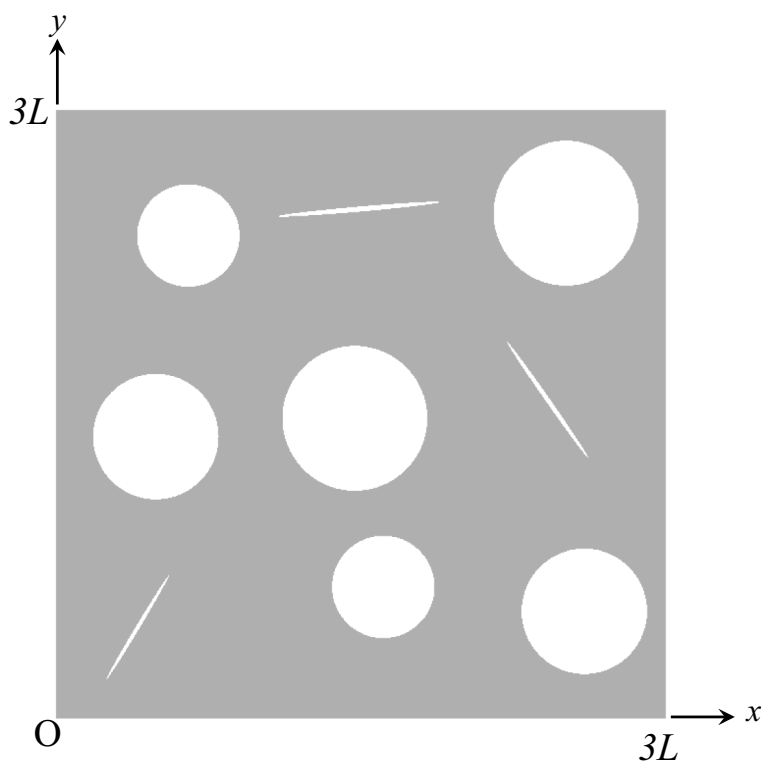
Fig. 4 Representative random pore/crack model containing six pores and three cracks in a $3L \times 3L$ domain ($D_c = 0.5D_p$). In this particular case, the average pore fraction $f_p = 0.2$ and the averaged normalized crack size $a/L = 0.29$

three-noded and four-noded linear heat transfer elements were employed. Mesh convergence was checked through various degrees of refinement. Verification of the computational model was demonstrated in our previous work, by comparing the simulation results with analytical solutions for select cases of pure pores and pure cracks (Shen et al. 2022a, 2022b). In the current study of steady-state heat transfer, the only material property needed is K_m. Values of the effective thermal conductivity are all presented in a normalized form, K_{eff}/K_m, so the results are applicable to all possible values of K_m at any temperature where K_m is valid.

Preliminary results: separate effects of periodic pores and periodic cracks

In this section, the numerical results based on the models in Figs. 1 and 2 are presented. The data were obtained from our previous work (Shen et al. 2022a, 2022b), and they are redrawn here to serve as the basis for the studies of the combined effects of pores and cracks presented in the following sections. The results for the pores-only case are presented in Fig. 6, with the effective thermal conductivity (normalized by the conductivity of the matrix, K_{eff}/K_m) as a function of the area fraction of the pores (f_p), for the four models

of uniform square array (Fig. 1a) and hexagonal array (Fig. 1b). It is evident that the reduction of thermal conductivity follows the same curve as the pore fraction increases. The primary conduction direction, as well as the spatial arrangement of periodic pores, do not cause any appreciable difference in the overall behavior. This observation is consistent with other numerical findings (Iasir et al. 2018; Wang and Zhao 2021). From our earlier study (Shen et al. 2022a), geometric clustering and coexistence of pores of different sizes were also found to have insignificant influence on the overall thermal conduction. The effective conductivity is thus dictated by the pore fraction.

Also shown as insets in Fig. 6 are the temperature distributions in the four models with a pore fraction of 0.15, with the blue color representing T_0 and the red color representing T_1 at the opposite boundaries. Note that in each model the temperature contours are independent of the actual temperature values used in the simulations (same blue-to-red distribution when different T_0 and T_1 values are assigned in the simulations). The calculated effective conductivity is based on Eq. (2) so a greater ($T_1 - T_0$) value will give rise to a proportionally higher reaction heat flux, which in turn leads to the same K_{eff}. It can be seen that the existence of pores disturbs the
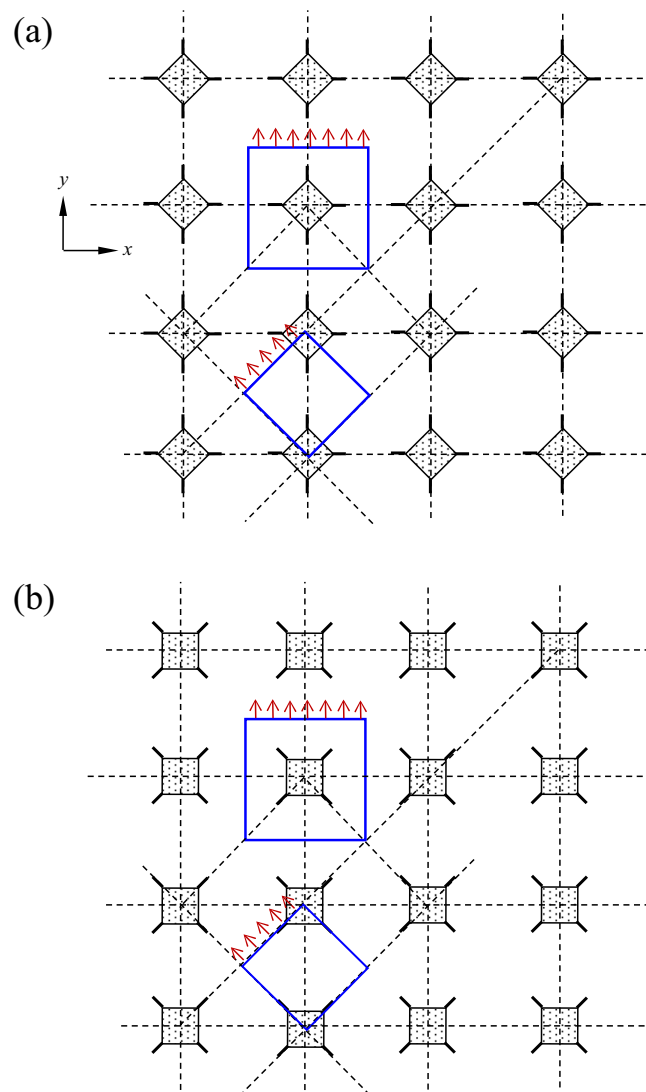
Fig. 5 Schematics showing periodic unit-cell models of cracks extended from the sharp corners of diamond-shaped (rotated square) pores (**a**) and square-shaped (properly oriented) pores (**b**). In each configuration two separate unit-cell models of the aligned and staggered arrangements can be analyzed as highlighted; they are designated as AD90, SD45, AS90, and SS45 from top to bottom

temperature field which would have been simple parallel color stripes for a homogeneous pore-free solid.

The effect of cracks is shown in Fig. 7 where the normalized effective thermal conductivity is plotted against the normalized crack size (a/L), for the three crack models of aligned square array with 0/90° direction (Fig. 2a) and staggered array with 0/90° and 45° directions (Fig. 2b). It is evident that the three models in Fig. 2, with evenly distributed and oriented cracks, lead to the same outcome. The insensitivity of effective thermal conduction to spatial distribution of cracks is not limited to the 0/90° and 45° directions in the aligned or staggered square arrays. Models with more random cracks, not just orientation distribution but also size variation, were also found to follow basically the same quantitative response (Shen et al. 2022b). It is the average normalized crack size (a/L) that determines the reduction in overall thermal conductivity. Figure 7 also includes four temperature contour maps obtained from the 45° staggered array simulations with a/L equal to 0.1, 0.2, 0.3, and 0.4. The blue and red colors at the boundaries again represent prescribed T_0 and T_1, respectively. The disturbance of temperature field due to the crack-induced discontinuity is evident, and its extent is greater if the crack is longer.
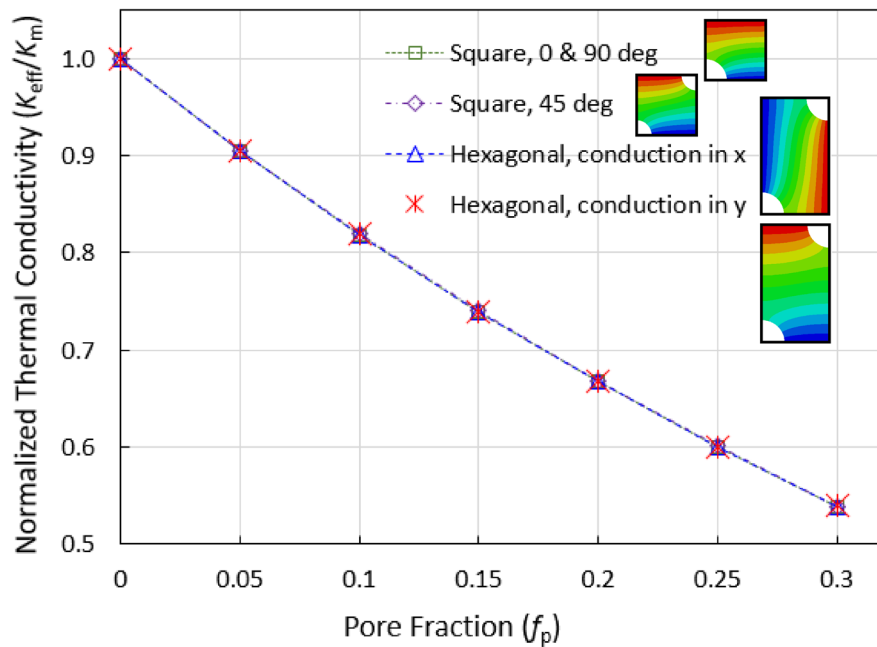
Shen and Rose *J Mater. Sci: Mater Eng.*   (2024) 19:25

Page 9 of 19

Fig. 6 Effective thermal conductivity, normalized by the conductivity of the matrix, as a function of area fraction of pores, for the four models of uniform square array (Fig. 1a) and hexagonal array (Fig. 1b). Shown as insets in the figure are the temperature distributions in the four models with a pore fraction of 0.15, with blue representing T_0 and red being T_1 at the opposite boundaries
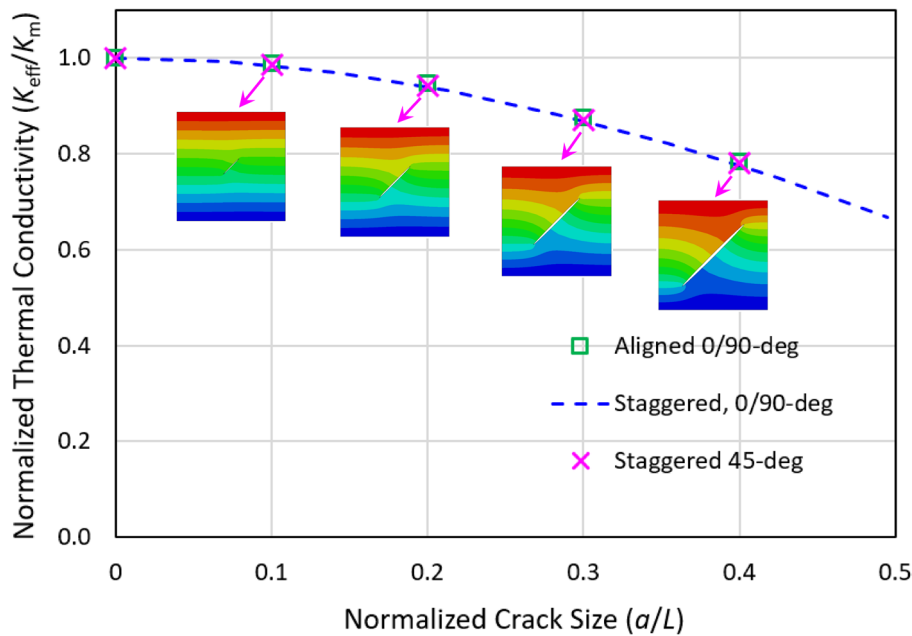

Fig. 7 Effective thermal conductivity, normalized by the conductivity of the matrix, as a function of the normalized crack size (a/L), for the three mixed-orientations crack models of aligned square array with 0/90° conduction direction (Fig. 2a), and staggered array with 0/90° and 45° directions (Fig. 2b)

Combined effects of periodic pores and cracks

The "Preliminary results: separate effects of periodic pores and periodic cracks" section established the baseline relationship between thermal conductivity and periodic pores or cracks. The modeling results with combined pores and cracks as depicted in Fig. 3

Shen and Rose *J Mater. Sci: Mater Eng.*   (2024) 19:25

Page 10 of 19

are now presented. The crack configurations in Figs. 3a and b correspond to those of Figs. 2a and b, respectively. This results in the same crack density and pore density ($D_c = D_p$) in Fig. 3a and only one-half the crack density ($D_c = 0.5D_p$) in Fig. 3b. Before showing the systematic numerical results, the representative temperature fields are first illustrated, and the resulting effective thermal conductivities based on the two forms of unit cells (0/90° vs. 45°) as highlighted in Fig. 3b are compared. The three temperature fields in Figs. 8a and b correspond to the one unit-cell model in Fig. 3a and two unit-cell models in Fig. 3b, respectively. The images shown are for the pore fraction $f_p = 0.2$ and normalized crack size $a/L = 0.4$. The primary heat conduction direction considered in these images is vertical. The disturbance of temperature field caused by the pores and cracks is evident. The simulated effective thermal conductivity as a function of pore fraction, for the two configurations in Fig. 8b, is shown in Fig. 8c. The 0/90° and 45° cases generate essentially the same K_{eff}, affirming the insensitivity to conduction direction with the combined periodic pores and cracks.

Systematic results for the models in Fig. 3 are now presented. The case of $D_c = D_p$ (Fig. 3a) is considered first, and its results are shown in Fig. 9a where the normalized effective thermal conductivity is plotted against the normalized crack size, under various pore fractions. When f_p is zero or small, the decrease in thermal conductivity caused by cracks is significant. For instance, at $f_p = 0.1$, the existence of cracks of size $a/L = 0.5$ will cause a reduction in K_{eff}/K_m from about 0.81 to 0.57. At larger f_p, the pore effect becomes more dominant so only a moderate decrease in K_{eff}/K_m caused by cracks can be observed (e.g., the curve of $f_p = 0.5$ is much less steep). The same thermal conductivity data in Fig. 9a can also be plotted as a function of pore fraction for various specified normalized crack sizes, shown in Fig. 9b. Note that the curve of $a/L = 0$ (no crack) is essentially the same as those shown in Fig. 6. With an increasing crack size (a/L), the thermal conductivity decreases further so the curves in Fig. 9b become lower. When the crack size is very large, the heat conduction pathways are much narrowed already so the variation of K_{eff}/K_m with pore fraction tends to be more moderate.

The results presented in Fig. 9 are for the case of $D_c = D_p$ (Fig. 3a). The same set of graphs can be shown for the case of $D_c = 0.5D_p$, as plotted in Figs. 10a and b, which correspond to the model configuration in Fig. 3b. Due to the smaller crack density, the thermal conductivity curves in Fig. 10 are all at a higher position than those in Fig. 9, except for the no-crack case of $a/L = 0$ in Fig. 10b which is the same as the topmost curve in Fig. 9b. However, the qualitative trends in Figs. 9 and 10 are the same.

The numerical results for the case of equal crack density and pore density, $D_c = D_p$, may be used to shed light on the relative influence of pores vs. cracks. One may consider, for instance, $f_p = 0.5$ (pores only) and use the pore's radius as the imaginary crack's half-length (for cracks only), which leads to $a/L \approx 0.4$. Then from Figs. 9a and b, f_p from 0 to 0.5 (no crack) results in a greater reduction in K_{eff}/K_m than a/L from 0 to 0.4 (no pore). Therefore, pores inside the material exert a greater influence than cracks in reducing the effective thermal conductivity.

More random distributions

To examine the generality of the periodic unit-cell approach, larger models with more randomly distributed pores and cracks are also analyzed. The results are shown in Figs. 11a and b, for the cases of $D_c = D_p$ and $D_c = 0.5D_p$, respectively. In the figures, the K_{eff}/K_m values obtained from the unit-cell models of $f_p = 0$, 0.1, and 0.2, taken from the data in Figs. 9 and 10, are plotted as a function of crack size (a/L) as dashed curves. Discrete points in Figs. 11a and b represent simulation results of more random pores and cracks for the corresponding pore fractions and crack sizes. Some pore/crack configurations and their temperature fields are shown as insets. Note that in a given model, the pores and cracks are not necessarily uniform in size; the discrete points shown in Fig. 11 are at positions corresponding to the *average* pore fractions and *average* crack sizes. It can be seen that the results of the random models largely follow those of the periodic unit cells. Slight deviations occur as the crack size and pore fraction become greater. Figures 11a and b thus attest to the generality of the simple unit-cell approach. It is also a manifestation that pores in the model have a greater influence than cracks in lowering the effective thermal conductivity, as discussed in the previous section.

The results presented in Figs. 9, 10, and 11 demonstrate that the coexistence of pores and cracks leads to further reduction in the effective thermal conductivity, compared to the cases of pores only and cracks only. It is worth noting that in actual experimental characterization of porous materials, porosity can be easily revealed by microscopic images, but the possible existence of cracks may be harder to discern. As a consequence, the overall thermal conductivity of the material may actually be lowered than what can be predicted from the apparent porosity. This may partially explain why there is frequently a large discrepancy in measured thermal conductivity values for materials with a given porosity (Smith et al. 2013; Kumar et al. 2019; Bowen et al. 2020).
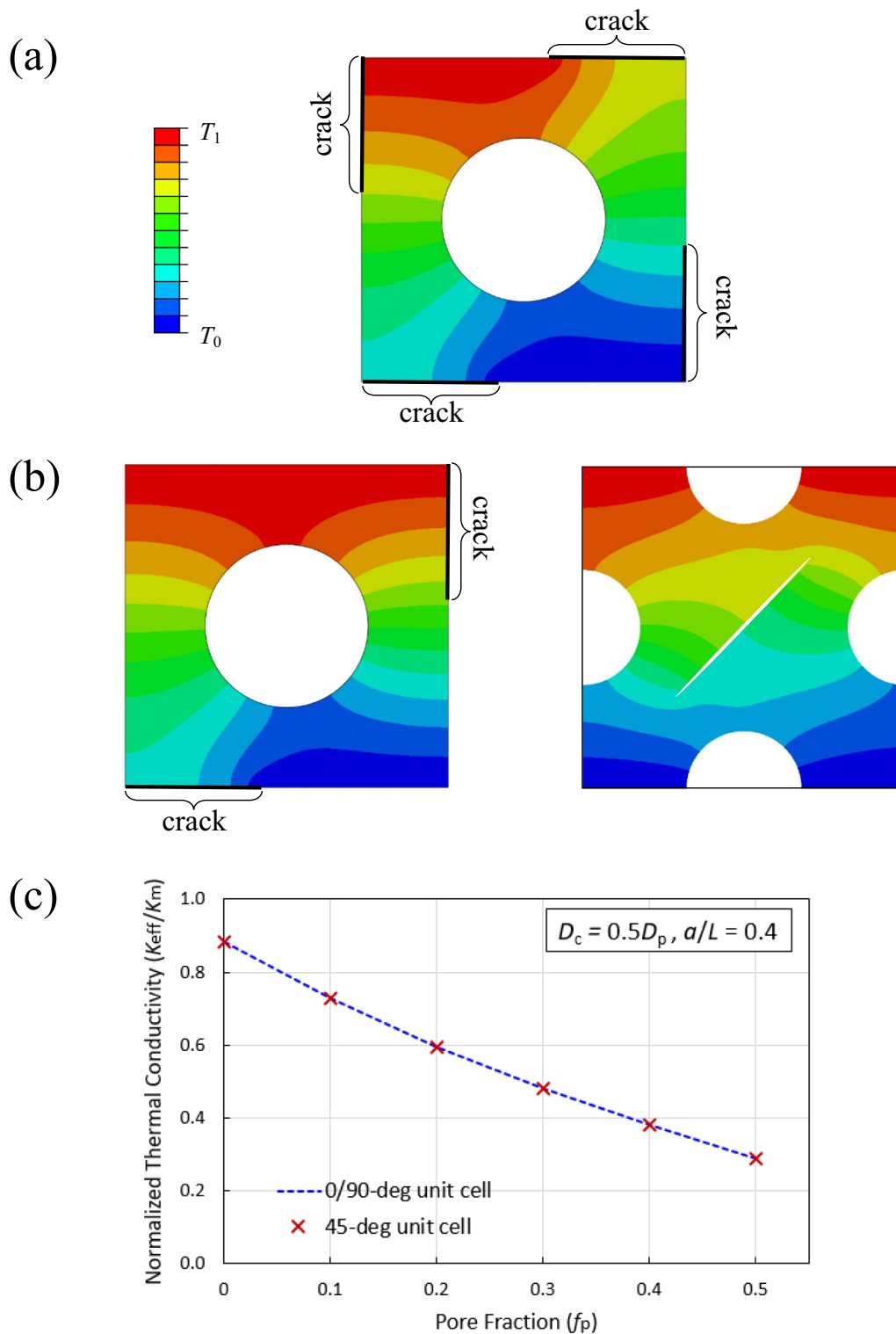
Fig. 8 Representative temperature fields obtained from the periodic unit-cell models of coexisting circular pores and cracks, with crack density being the same as pore density ($D_c = D_p$, Fig. 3a) (**a**), and crack density being one-half of pore density ($D_c = 0.5D_p$, Fig. 3b) (**b**). Note that the bounding temperatures T_0 and T_1 can be any low- and high-temperature values used in the modeling. The images shown correspond to the pore fraction $f_p = 0.2$ and normalized crack size $a/L = 0.4$. **c** Comparison of normalized effective thermal conductivity values as a function of pore fraction (f_p), for $D_c = 0.5D_p$ and $a/L = 0.4$, using the 0/90° and 45° unit-cell models

Shen and Rose *J Mater. Sci: Mater Eng.*   (2024) 19:25

Page 12 of 19

(a)

(b)
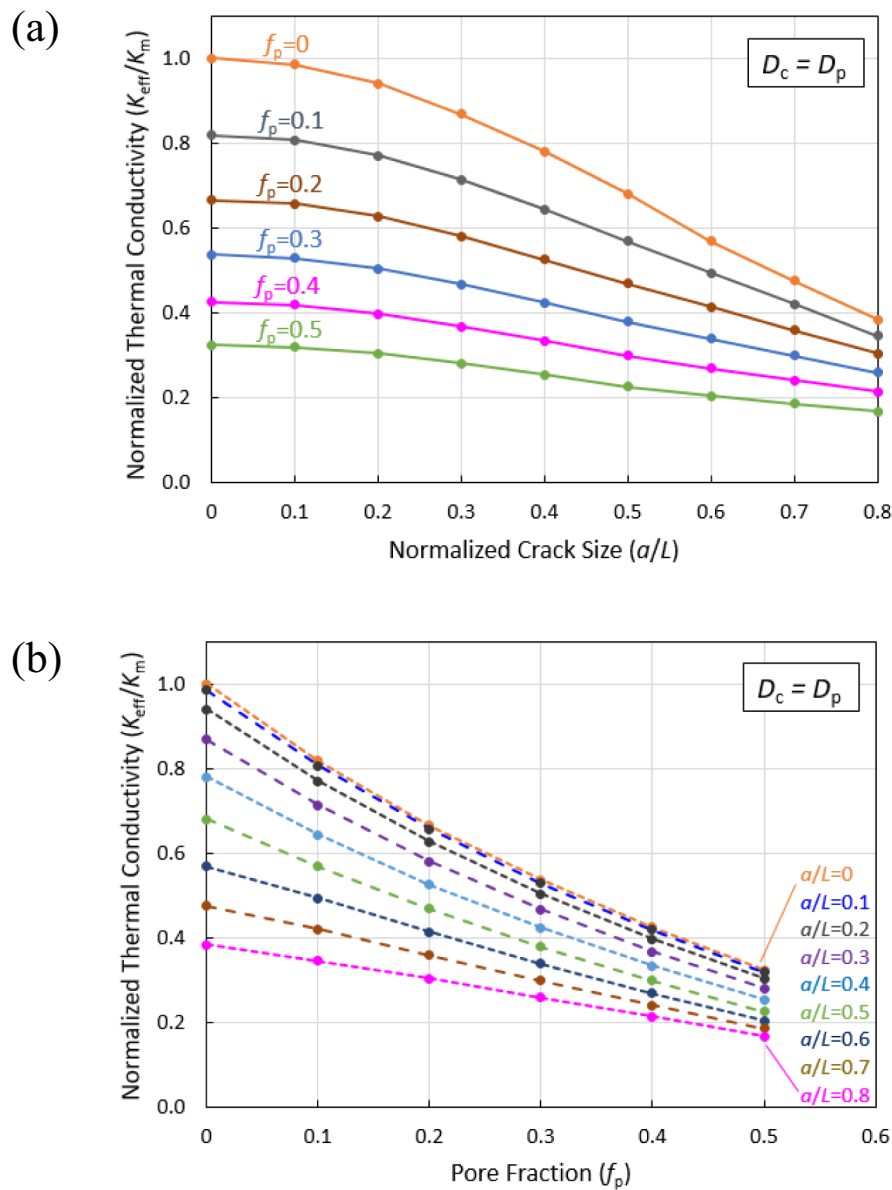
Fig. 9 Normalized effective thermal conductivity (K_{eff}/K_m) as a function of normalized crack size (a/L) for various pore fractions (f_p) from 0 to 0.5 (**a**) and normalized pore fraction for various normalized crack sizes from 0 to 0.8 (**b**), when the crack density (D_c) is equal to pore density (D_p)

Cracks extended from angular pores

Attention is now turned to angular pores with diamond and square shapes, with possible cracks extending from the sharp corners as depicted in Figs. 5a and b. Four unit-cell geometries, aligned diamond shape (AD90), staggered diamond (SD45), aligned square (AS90), and staggered square (SS45), were identified in Fig. 5. In the analyses presented below, equal lengths of the cracks from all corners of the pore along the two mutually perpendicular directions in each model are considered. The crack size is expressed as a normalized quantity of actual

crack extension divided by the unit-cell span along the crack directions (horizontal, vertical, or diagonal). The reference cases with pores only are characterized first.

Figure 12 shows the effective normalized thermal conductivity as a function of pore fraction, for the four model configurations with pores only (no crack). For reference purposes, the result from the models of circular pores, taken from Fig. 6, is also included in the figure. It can be seen that the AD90 and SD45 models generate essentially identical thermal conductivity values for a given pore fraction. AS90 and SS45 display a similar
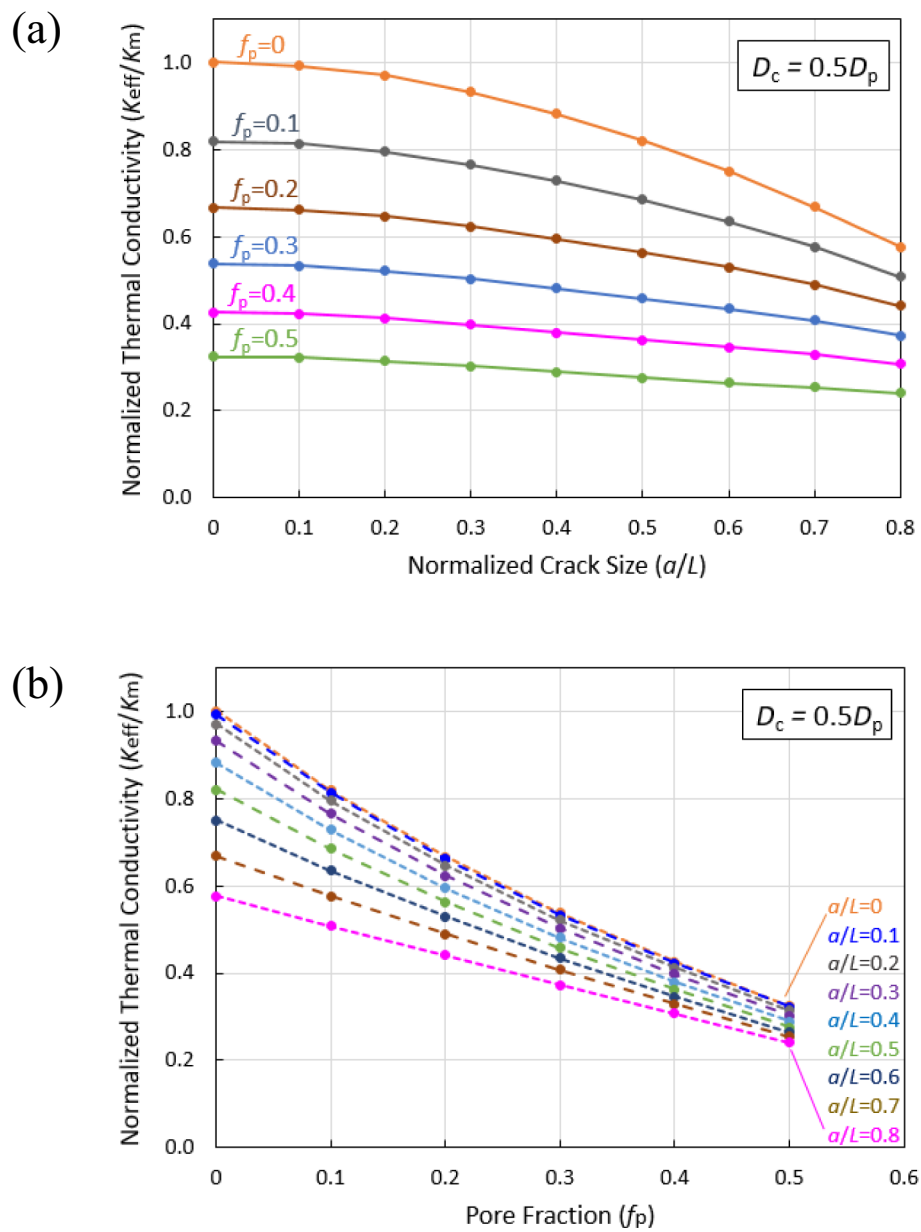
(a)

(b)

Fig. 10 Normalized effective thermal conductivity (K_{eff}/K_m) as a function of normalized crack size (a/L) for various pore fractions (f_p) from 0 to 0.5 (**a**) and normalized pore fraction for various normalized crack sizes from 0 to 0.8 (**b**), when the crack density (D_c) is equal to 0.5 pore density (D_p)

type of orientation-independent behavior. When f_p is smaller than about 0.2, all four models show very close thermal conductivities; beyond the 0.2 pore fraction, the diamond-shaped pores lead to lower conductivities. This is due to the fact that the diamond shape possesses a wider span (diagonal direction) perpendicular to the primary heat conduction direction, thus imposing greater blockage of conductive pathways. Note also that all four models with diamond or square-shaped pores result in moderately lower K_{eff}/K_m compared to that of circular

pores. This trend is consistent with analyses reported in other studies (Yang et al. 2013).

With the reference cases of pores-only established, the presentation now focuses on how the extension of cracks will further degrade the thermal conduction behavior. Figure 13 shows the normalized effective thermal conductivity as a function of the normalized crack extension, for the models of (a) AD90, (b) SD45, (c) AS90, and (d) SS45. In all cases, the pore fractions of $f_p = 0.1$, 0.2, and 0.3 are included. In each model, a representative temperature
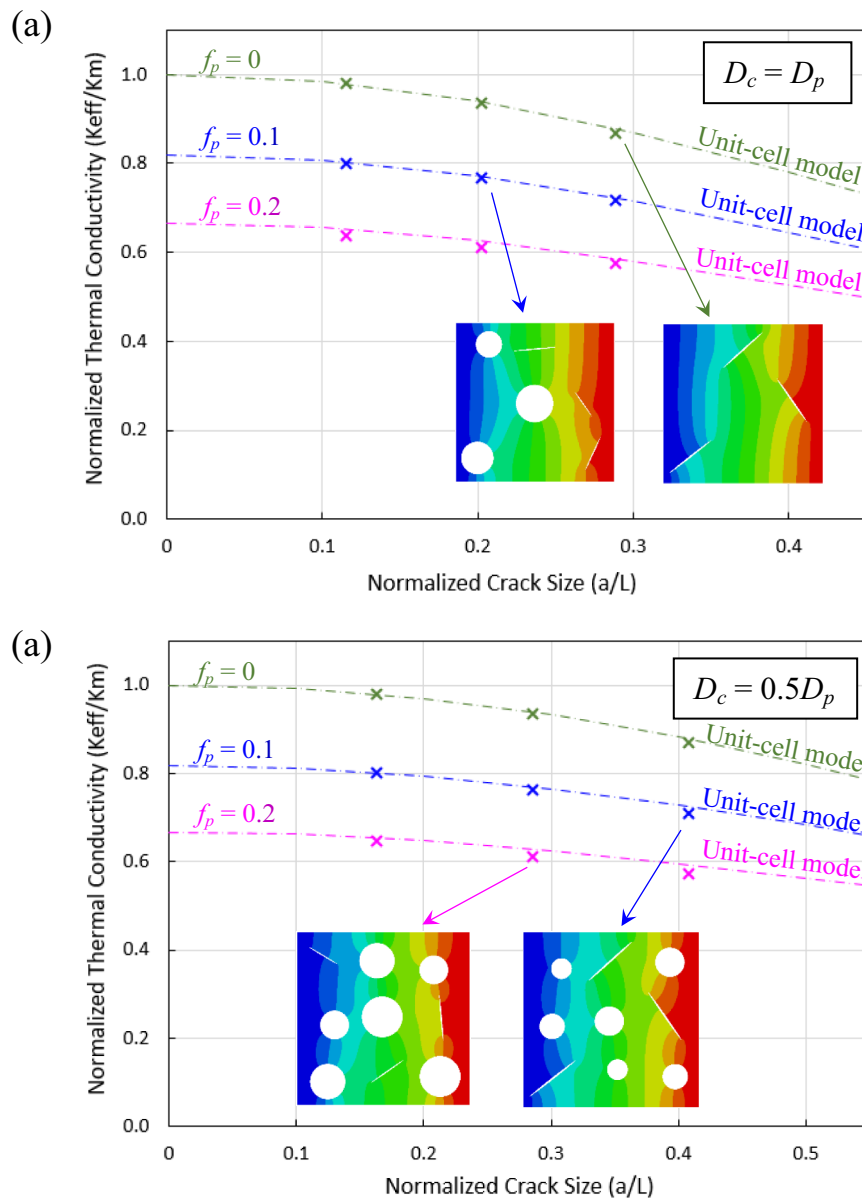
Shen and Rose *J Mater. Sci: Mater Eng.*   (2024) 19:25

Page 14 of 19

(a)

(a)

Fig. 11 Comparisons of periodic unit-cell results (dashed lines) and the randomly distributed models (× symbols). When the crack density (D_c) is equal to the pore density (D_p) (**a**); when the crack density (D_c) is one-half of the pore density (D_p) (**b**). Also shown as insets are representative model configurations of random pores and cracks and their temperature fields

contour plot with the corresponding pore/crack configuration is included as an inset. Note that the last points in all curves are shown in Figs. 13a–d correspond to an overall crack/pore span (from the crack tip through the center pore to the other crack tip) of 80% of the unit-cell span along the same direction. As a consequence, in each plot the curves of $f_p = 0.1$, 0.2, and 0.3, all have different lengths (the larger pore has a longer diagonal and thus the maximum crack extension will be smaller). It can be seen that the existence of cracks further decreases the

effective conductivity. Care should thus be taken when deducing thermal conductivity from the apparent porosity obtained microscopically, since cracks evolving from the pore corners may exist especially in additively manufactured materials due to relatively poor adhesion. Also observed in Figs. 13a–d is that, in each figure, the last point of $f_p = 0.3$ has the lowest K_{eff}/K_m compared to the last points of $f_p = 0.2$ and then 0.1. This suggests that the embedded pores lead to more significant reduction of thermal conductivity than the extended cracks since the
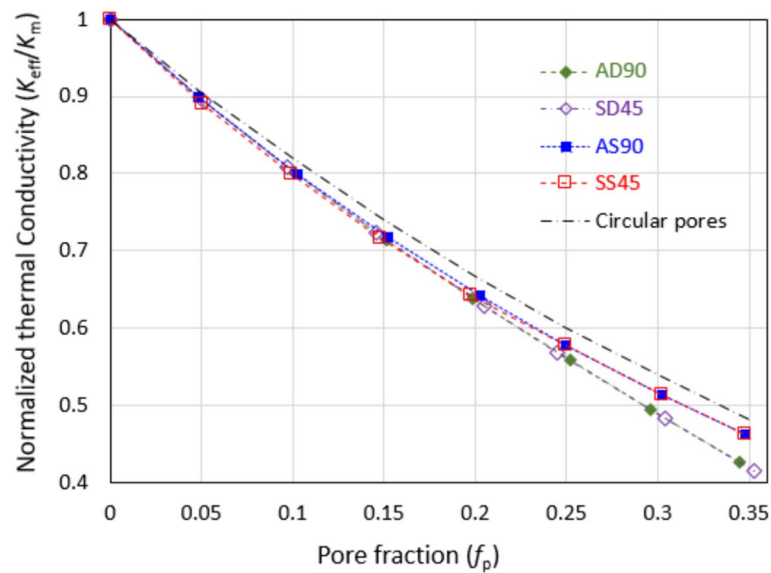
Fig. 12 Effective thermal conductivity, normalized by the conductivity of the matrix, as a function of area fraction of pores, for the four pores-only models (no crack) of AD90, SD45, AS90, and SS45 defined in Fig. 5. For comparison, a reference curve from the circular pore model (shown in Fig. 6) is included

last points in all the curves in Fig. 13 correspond to the same normalized span of 0.8. Further illustrations of the tendency are presented in Fig. 14.

Comparing the different models shown in Fig. 13, it is also evident that, as the crack length increases to reach the 80% tip-to-tip crack/pore span, AS90 and SS45 (Figs. 13c and d) display a greater reduction in thermal conductivity than AD90 and SD45 (Figs. 13a and b). This observation implies different geometric effects of the cracks in blocking the heat flow for the two sets of models. Figure 14 compares the pores-only (no crack) results with those of cracks-only (no pore). Due to the essentially identical behavior between AD90 and SD45 and between AS90 and SS45, only the two models AD90 and AS90 are included, and the tip-to-tip (diagonal) span is used to represent the sizes of the pore and cross-shaped cracks in a unified manner. In each configuration of AD90 and AS90, the pore model (no crack) is seen to result in a lower curve than the crack model (no pore), thus illustrating again the larger effect of the pores on overall thermal conductivity. AS90 tends to reduce the conductivity more, which is consistent with the general trend observed in Fig. 13. This is due to the fact that, at any given normalized tip-to-tip span, there is either a crack parallel to the primary heat flow direction (thus not contributing to blocking the primary conduction path) or a pore with a smaller area fraction, for the AD90 model compared to AS90 (see the geometric layout in Fig. 5).

The results presented in Figs.13 and 14, as well as those in previous sections, illustrated that internal cracks can

significantly impact the effective thermal conductivity, regardless if the cracks are isolated or connected to the existing pore.

Although the current study is devoted to the periodic arrays of pores and cracks, qualitative comparisons with experiments with realistic microstructures can still be attempted. Figure 15 includes some measured effective thermal conductivities as a function of pore fraction, taken from the literature, for various material systems (Koh and Fortini 1973; Nosewicz et al. 2022; Simmons et al. 2020; Smith et al. 2003; Živcová et al. 2009). The figure also includes representative simulations from the current study, based on circular pores and square-shaped pores (AS90 with no crack), as well as square-shaped pores with extended cracks (AS90 with extended cracks of normalized crack extension of 0.2). Note that the simulation curves as shown have been adjusted using a 2D/3D conversion relation (Bakker et al. 1995), which was validated in Shen et al. 2022a,

$$\frac{1 - f_p - \left(\frac{K_{eff}}{K_m}\right)_{2d}}{1 - f_p - \left(\frac{K_{eff}}{K_m}\right)_{3d}} = 1.8. \tag{3}$$
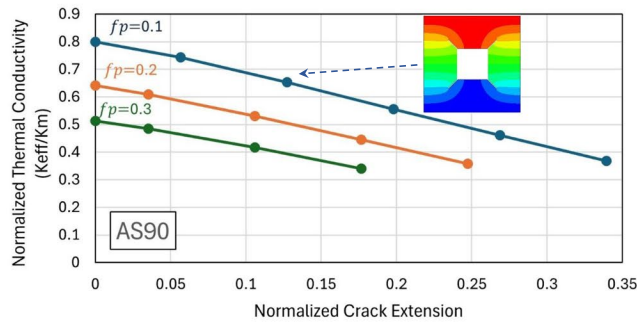
It is evident from Fig. 15 that a great extent of scatter exists in the measurements. While there may not be a direct correspondence between simulations and actual measurements in Fig. 15, the relative positions of the simulation curves and experimental distributions nevertheless point to the possibility of internal cracks as an
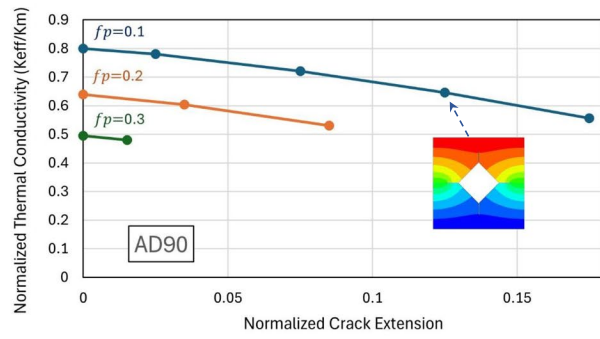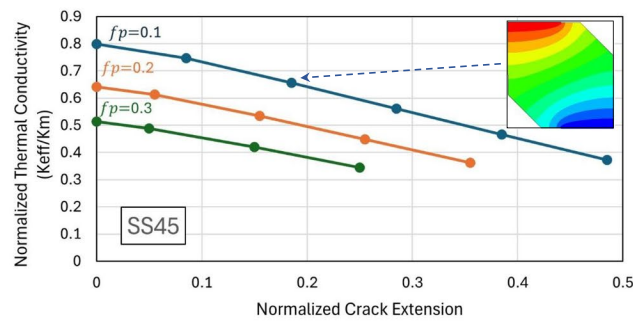
(a)
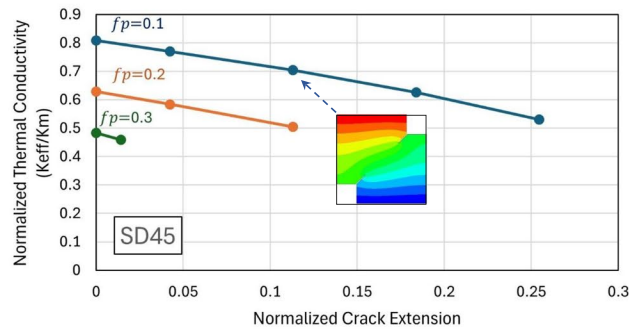
(b)

(c)

(d)

Fig. 13 Effective thermal conductivity (normalized by the conductivity of the matrix) as a function of crack extension (normalized by the side length of the unit cell), for the models of AD90 (**a**), SD45 (**b**), AS90 (**c**), and SS45 (**d**). A representative temperature contour plot is included as inset in each case. In each model, three different pore fractions (f_p = 0.1, 0.2, and 0.3) are presented
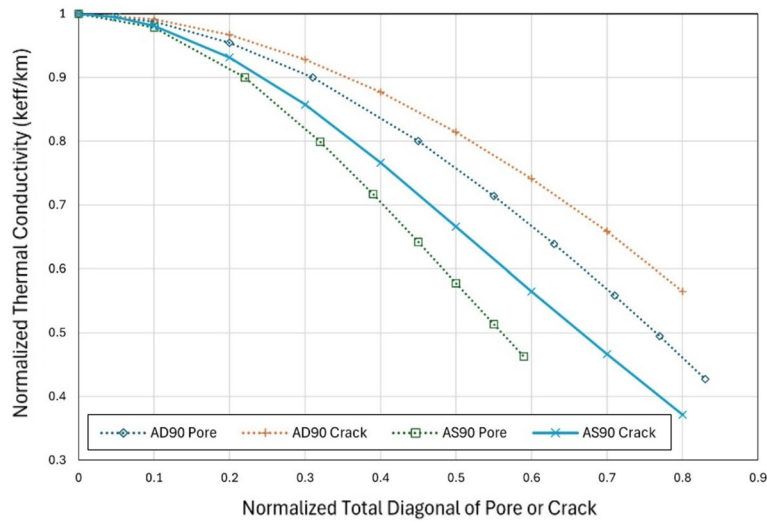
Fig. 14 Effective thermal conductivity, normalized by the conductivity of the matrix, as a function of normalized crack span, for the models of AD90 pore-only, AD90 crack-only, AS90 pore-only, and AS90 crack-only. Note that for the pore-only cases, the normalized diagonal span is used to represent the size of the pore so a unified comparison with the crack-only cases can be made
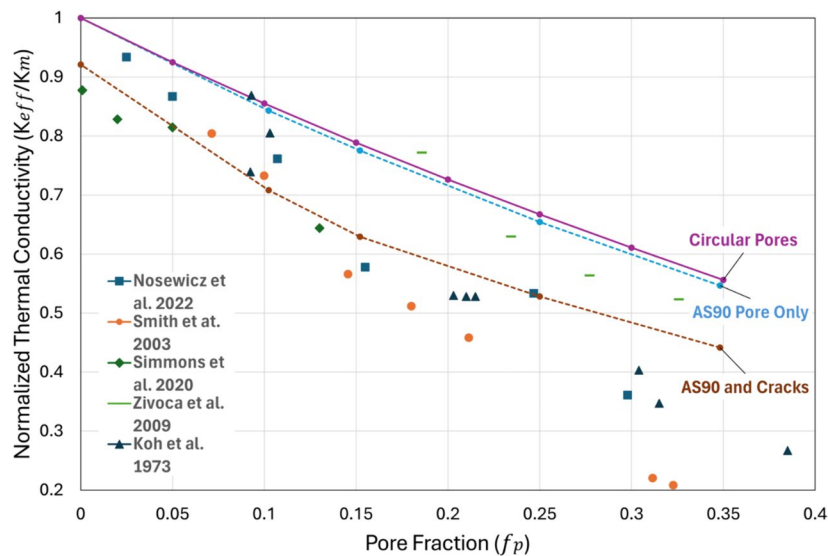
Fig. 15 Representative simulation results (circular pores with no crack, AS90 model with pore only, and AS90 model with extended crack of normalized length of 0.2) plotted with some experimental measurements reported in the literature. The simulation curves have been adjusted using a 2D/3D conversion relation described in the text

important factor in lowering the effective thermal conductivity of porous media.

Conclusions

Systematic numerical finite-element analyses were conducted, to study the combined effects of internal pores and cracks on the effective thermal conductivity of two-dimensional solids. Periodic models of intermixed circular pores and sharp cracks, as well as square- or diamond-shaped pores with cracks extending from the sharp corners, were studied. Salient findings are summarized below.

- Both the isolated cracks and cracks connected to existing pores can significantly reduce the effective thermal conductivity in porous materials. Since bulky voids are much easier to detect, microscopically or using density measurement, than sharp cracks, care

Shen and Rose *J Mater. Sci: Mater Eng.*   (2024) 19:25

Page 18 of 19

should be taken in using the apparent porosity to estimate the overall thermal conductivity.

- For models containing only circular pores, the effective thermal conductivity is dictated by the pore fraction and is insensitive to the geometric distribution and orientation of the pores. For models containing only cracks, the effective thermal conductivity is also insensitive to the crack layout and is largely controlled by the normalized crack size and density. The coexistence of pores and cracks results in similar features, with the crack density relative to the pore density playing an additional role.
- More randomly distributed pores and cracks showed quantitatively similar results to those of the periodic counterparts, demonstrating the generality of the regular unit-cell approach considered in this study.
- With cracks extending from the sharp corners of pores, the unit-cell models considered in this study also showed a high degree of generality, as the aligned and staggered arrangements resulted in very close conductivity values for a given diamond or square pore configuration. Thermal conductivity is not solely determined by the overall tip-to-tip crack spans; the pore at the crack center also contributes to lowering the effective thermal conductivity.

The simulations conducted in this study are valid for uniform arrays of pores and/or cracks covering the entire two-dimensional body. If there is significant clustering of pores and/or cracks with a large area of material otherwise free of defects, the problem will be less well defined and a case-by-case analysis will be necessary. Future developments may also include direct simulations of the complex three-dimensional geometries.

Authors' contributions
YLS conceived the idea, supervised the research, and wrote the original draft. YLS and GR performed the numerical simulations and analyses, and contributed to finalizing the manuscript.

Availability of data and materials
All data generated and analyzed during this study are included in this published article.

Declarations

Competing interests
The authors declare that they have no competing interests.

References

Abdulagatova ZZ, Abdulagatov IM, Emirov SN (2010) Effect of pressure, temperature, and oil-saturation on the thermal conductivity of sandstone up to 250 MPa and 520 K. J Petroleum Sci Engng 73:141–155

Amran YHM, Farzadnia N, Abang Ali AA (2015) Properties and applications of foamed concrete; a review. Constr Build Mater 101:990–1005

Atabaki N, Baliga BR (2007) Effective thermal conductivity of water-saturated sintered powder-metal plates. Heat Mass Transfer 44:85–99

Bai X-M, Tonks MR, Zhang Y, Hales JD (2016) Multiscale modeling of thermal conductivity of high burnup structures in UO$_2$ fuels. J Nucl Mater 470:208–215

Bakker K, Kwast H, Cordfunke EHP (1995) Determination of a porosity correction factor for the thermal conductivity of irradiated UO2 fuel by means of the finite element method. J Nucl Mater 226:128–143

Bauer TH (1993) A general analytical approach toward the thermal conductivity of porous media. Int J Heat Mass Transfer 36:4181–4191

Benveniste Y, Miloh T (1989) An exact solution for the effective thermal conductivity of cracked bodies with oriented elliptical cracks. J Appl 66(1):176–180

Bidare P, Jimenez A, Hassanin H, Essa K (2022) Porosity, cracks, and mechanical properties of additively manufactured tooling alloys: a review. Adv Manuf 10:175–204

Bowen CR, Robinson K, Tian J, Zhang M, Coveney VA, Xia Q, Lock G (2020) The emergent behavior of thermal networks and its impact on the thermal conductivity of heterogeneous materials and systems. J Composites Sci 4:32

Byun TS, Gussev MN, Lach TG (2024) Deformation and fracture behavior of additively manufactured 316L stainless steel. JOM 76:362–378

Carson JK, Lovatt SJ, Tanner DJ, Cleland AC (2003) An analysis of the influence of material structure on the effective thermal conductivity of theoretical porous materials using finite element simulations. Int J Refrigeration 26:873–880

Chiew YC, Glandt E (1983) The effect of structure on the conductivity of a dispersion. J Colloid Interface Sci 94:90–104

Dinesh BVS, Bhattacharya A (2019) Effect of foam geometry on heat absorption characteristics of PCM-metal foam composite thermal energy storage systems. Int J Heat Mass Transf 134:866–883

Dou L, Zhang X, Cheng X, Ma Z, Wang X, Si Y, Yu J (2019) Ding B (2019) Hierarchical cellular structured ceramic nanofibrous aerogels with temperature-invariant superelasticity for thermal insulation. ACS Appl Mater Interfaces 11(32):29056–29064

Ghorbani J, Koirala P, Shen Y-L, Tehrani M (2022) Eliminating voids and reducing mechanical anisotropy in fused filament fabrication parts by adjusting the filament extrusion rate. J Manuf Process 80:651–658

Gu S, Lu TJ, Hass DD, Wadley HNG (2001) Thermal conductivity of zirconia coatings with zig-zag pore microstructures. Acta Mater 49(13):2539–2547

Hashemi SM, Parvizi S, Baghbanijavid H et al (2022) Computational modelling of process–structure–property–performance relationships in metal additive manufacturing: a review. Int Mater Rev 67:1–46

Hashin Z, Shtrikman S (1962) A variational approach to the theory of the effective magnetic permeability of multiphase materials. J Appl Phys 33(10):3125–3131

Hasselman DPH (1978) Effect of cracks on thermal conductivity. J Compos Mater 12:403–407

Hawkes GL, Sterbentz JW, Maki JT, Pham BT (2017) Thermal predictions of the AGR-3/4 experiment with post irradiation examination measured time-varying gas gaps. J Nucl Eng Radiat Sci 3:041007

He Y, Guo J, Yang H (2019) Image-based numerical prediction for effective thermal conductivity of heterogeneous materials: a quadtree based scaled boundary finite element method. Int J Heat Mass Transfer 128:335–343

Hoenig A (1983) Thermal conductivities of a cracked solid. J Compos Mater 17:231–237

Hsu CT, Cheng P, Wong KW (1995) A lumped-parameter model for stagnant thermal conductivity of spatially periodic porous media. J Heat Transfer 117:264–269

Shen and Rose *J Mater. Sci: Mater Eng.*   (2024) 19:25

Page 19 of 19

Iasir ARM, Peters NJ, Hammond KD (2018) Estimation of effective thermal conductivity in U-10Mo fuels with distributed xenon gas bubbles. J Nucl Mater 508:159–167

Ibrahim Y, Elkholy A, Schofield JS, Melenka GW, Kempers R (2020) Effective thermal conductivity of 3D-printed continuous fiber polymer composites. Adv Manuf Polym Compos Sci 6(1):17–28

Kaddouri W, El Moumen A, Kanit T et al (2016) On the effect of inclusion shape on effective thermal conductivity of heterogeneous materials. Mech Mater 92:28–41

Kaviany M (1991) Principles of heat transfer in porous media. Springer-Verlag, New York

Kiradjiev KB, Halvorsen SA, Van Gorder RA, Howison SD (2019) Maxwell-type models for the effective thermal conductivity of a porous material with radiative transfer in the voids. Int J Therm Sci 145:106009

Koh JCY, Fortini A (1973) Prediction of thermal conductivity and electrical resistivity of porous metallic materials. Int J Heat Mass Transf 16:2013–2022

Kubota T, Seki Y, Takahashi S (1964) Thermal conductivity of UO_2, UC and UC_2. J Nucl Sci Technol 1(3):93–100

Kushch VI, Sangani AS (2000) Conductivity of a composite containing uniformly oriented penny-shaped cracks or perfectly conducting discs. Proc R Soc Lond A 456:683–699

Landauer R (1952) The electrical resistance of binary metallic mixtures. J Appl Phys 23:779–784

Loeb AL (1954) Thermal conductivity: VIII, A theory of thermal conductivity of porous materials. J Am Ceram Soc 37:96–99

Lu TJ, Stone HA, Ashby MF (1998) Heat transfer in open-cell metal foams. Acta Metall 46(10):3619–3635

Marr J, Zartmann L, Reinel-Bitzer D, Andra H, Muller R (2022) Parametric optimization of the effective thermal conductivity for a three-phase particle-filled composite. Computational Mater Sci 205:111214

Maxwell JC (1873) A treatise on electricity and magnetism. Clarendon Press, Oxford

Nguyen ST, Vu M-H, Vu MN et al (2017) Modeling of heat flow and effective thermal conductivity of fractured media: analytical and numerical methods. J Appl Geophys 140:117–122

Nosewicz S, Jurczak G, Wejrzanowski T et al (2022) Thermal conductivity analysis of porous nial materials manufactured by spark plasma sintering: experimental studies and modelling. Int J Heat Mass Transf 194:123070

Ogushi T, Chiba H, Nakajima H, Ikeda T (2004) Measurement and analysis of effective thermal conductivities of lotus-type porous copper. J Appl Phys 95:5843–5847

Ordonez-Miranda J, Alvarado-Gil JJ (2012) Effect of the pore shape on the thermal conductivity of porous media. J Mater Sci 47:6733–6740

Pietrak K, Wisniewski TS (2015) A review of models for effective thermal conductivity of composite materials. J Power Technol 95(1):14–24

Qin F, Hu Y, Dai Y, An T, Chen P, Gong Y, Yu H (2020) Crack effect on the equivalent thermal conductivity of porously sintered silver. J Electron Mater 49(10):5994–6008

Rangasamy Mahendren SR, Welemane H, Dalverny O et al (2020) Steady-state heat transfer in microcracked media. Mech Industry 21:519

Rankouhi B, Javadpour S, Delfanian F, Letcher T (2016) Failure analysis and mechanical characterization of 3D printed ABS with respect to layer thickness and orientation. J Fail Anal Prev 13(3):467–481

Rayleigh L (1892) On the influence of obstacles arranged in rectangular order upon the properties of medium. Philos Mag 5:481–502

Renteria AF, Saruhan B, Schulz U, Raetzer-Scheibe HJ, Haug J, Wiedenmann A (2006) Effect of morphology on thermal conductivity of EB-PVD PYSZ TBCs. Surf Coat Technol 201(6):2611–2620

Rutqvist J, Wu YS, Tsang C-F, Bodvarsson G (2002) A modeling approach for analysis of coupled multiphase fluid flow, heat transfer, and deformation in fractured porous rock. Int J Rock Mech Min Sci 39(4):429–442

Schulz B (1981) Thermal conductivity of porous and highly porous materials. High Temp High Press 13(6):649–660

Sevostianov I (2006) Thermal conductivity of a material containing cracks of arbitrary shape. Int J Engng Sci 44:513–528

Shen Y-L, Abdo MG, Van Rooyen IJ (2022a) Numerical study of effective thermal conductivity for periodic closed-cell porous media. Transp Porous Media 143:245–269

Shen Y-L, Abdo MG, Van Rooyen IJ (2022b) Thermal conductivity of crack-containing media: a numerical study. J Composite Mater 56:2495–2508

Simmons JC, Chen X, Azizi A et al (2020) Influence of processing and microstructure on the local and bulk thermal conductivity of selective laser melted 316L stainless steel. Addit Manuf 32:100996

Smith DS, Fayette S, Grandjean S et al (2003) Thermal resistance of grain boundaries in alumina ceramics and refractories. J Am Ceram Soc 86:105–111

Smith DS, Alzina A, Bourret J et al (2013) Thermal conductivity of porous materials. J Mater Res 28:2260–2272

Sun Q, Rizvi GM, Bellehumeur CT, Gu P (2008) Effect of processing conditions on the bonding quality of FDM polymer filaments. Rapid Prototyping J 14(2):72–80

Sun Z, Guo W, Jorgensen AB (2024) A computational multiscale modeling method for nanosilver-sintered joints with stochastically distributed voids. J Electron Mater 53:2437–2454

Wang Y, Zhao J (2021) Numerical simulations of thermal conductivity in void-containing tungsten: topological feature of voids. J Nucl Mater 543:152601

Xiong Z, Wang X, He M, Benabou L, Feng Z (2022) Investigation on thermal conductivity of silver-based porous materials by finite difference method. Mater Today Commun 33:104897

Xu W, Zhang Y, Jiang J, Liu Z, Jiao Y (2021) Thermal conductivity and elastic modulus of 3D porous/fractured media considering percolation. Int J Engng Sci 161:103456

Yang X, Lu T, Kim T (2013) Effective thermal conductivity modelling for closed-cell porous media with analytical shape factors. Transp Porous Med 100:211–224

Yap T, Heathman N, Phillips T, Beaman J, Tehrani M (2023) Additive manufacturing of polyaryletherketone (PAEK) polymers and their composites. Compos B 266:111019

Yeap K-B, Kopycinska-Mueller M, Chen L et al (2013) The effect of the pore topology on the elastic modulus of organosilicate glasses. J Mater Res 28:1262–1268

Yegyan Kumar A, Wang J, Bai Y et al (2019) Impacts of process-induced porosity on material properties of copper made by binder jetting additive manufacturing. Mater Des 182:108001

Yvonnet J, He Q-C, Toulemonde C (2008) Numerical modelling of the effective conductivities of composites with arbitrarily shaped inclusions and highly conducting interface. Compos Sci Technol 68:2818–2825

Zhang C, Wu Y, He Y et al (2021) Investigation on thermo-mechanical performance of fully ceramic microencapsulated fuel. J Nucl Mater 556:153171

Zhang S, Lane B, Whiting J, Chou K (2018) An investigation into metallic powder thermal conductivity in laser powder bed fusion additive manufacturing. Proceedings of the Solid Freeform Fabrication Symposium, Austin, 2018.

Zhao Z, Zhang H, Zou G, Ren H, Zhuang W, Liu L, Zhou YN (2019) A predictive model for thermal conductivity of nano-Ag sintered interconnect for a SiC die. J Electron Mater 48(5):2811–2825

Zhou H, Liu H, Hu D, Zhang F, Yang F, Lu J (2016) Estimation of the effective thermal properties of cracked rocks. European J Environmental Civil Engng 20:954–970.

Zhu W, Cai XN, Yang L, Xia J, Zhou YC, Pi ZP (2019) The evolution of pores in thermal barrier coatings under volcanic ash corrosion using X-ray computed tomography. Surf Coat Technol 357:372–378

Živcová Z, Gregorová E, Pabst W et al (2009) Thermal conductivity of porous alumina ceramics prepared using starch as a pore-forming agent. J Eur Ceram Soc 29:347–353

Publisher's Note